

ADVANCED ECG PROCESSING FOR CARDIAC MRI IN
ARRHYTHMIA

by
Shuo Han

A thesis submitted to Johns Hopkins University in conformity with the requirements for
the degree of Master of Science and Engineering

Baltimore, Maryland
May, 2016

© 2016 Shuo Han
All Rights Reserved

Abstract

Arrhythmia commonly compromises the quality of standard cardiac MRI (CMR), and cine CMR of arrhythmias may be of interest for evaluating arrhythmia pathophysiology. The common method to perform MRI during arrhythmia is real-time imaging; however, temporal and spatial resolution is limited. In this work, a triggered method utilizing a newly implemented triggering system and a retrospectively gated method were evaluated. The triggering system was capable of both classifying the heartbeat type in real-time from an ECG signal and triggering the scanner to update the k-space sampling trajectory when a pre-chosen heartbeat type was encountered. On the other hand, the retrospectively gated method analyzes the ECG signal after imaging is completed and selects the appropriate k-space data to use in reconstruction. Numerical simulations incorporating different paces of heartbeats and respiration were performed to compare the efficiency of both methods. The triggered and the retrospectively gated methods were also evaluated in an animal experiment, and k-space sampling patterns of selected imaging data and reconstructed images are shown. The numerical simulations and the animal experiment suggested the higher time-efficiency of the triggered method compared with the retrospectively gated method. This work provided a platform where high temporal and spatial resolution CMR imaging could be performed, enabling studies of arrhythmic pathophysiology using MRI.

Readers: Dr. Daniel Herzka, Dr. Aravindan Kolandaivelu, and Dr. Jerry L. Prince

Acknowledgments

I would like to express my deepest appreciation to Dr. Kolandaivelu and Dr. Herzka. This thesis would have not been possible without their guidance and support.

Preface

The thesis is an original work of the author, Shuo Han. This work was based on a physiologic signal acquisition and scanner synchronization system, a programmable MR scanner triggering system, a programmable animal pacing system, and a trigger-able segmented radial steady-state free precession MRI sequence developed by Dr. Aravindan Kolandaivelu. The rest of the work, including real-time heartbeat detection, classification, and selection software, simulations, image reconstruction, and statistical analysis, was implemented by the author, Shuo Han.

Contents

Abstract	ii
Acknowledgments	iii
Preface	iv
List of Tables	viii
List of Figures	ix
Introduction	1
1. Motivation.....	1
2. Background.....	2
Signal excitation.....	2
Spatial information encoding and k-space	3
MRI sequence and k-space sampling trajectory.....	5
Image reconstruction.....	6
Cine imaging	7
Methods	9
3. Physiologic-signal acquisition	9
4. Beat-type detection in real-time and triggering signal generation.....	10
Detection of QRS complexes.....	10
Classification of beat-types	12
Evaluation of QRS complex detection and beat-type classification	14

Detection of end-expiration.....	15
Trigger generation.....	15
5. Design of imaging sequences.....	16
Triggered beat-type imaging sequence design.....	16
Retrospectively gated beat-type imaging sequence design.....	19
6. Numerical simulations	22
7. Beat-type imaging experiment design	23
8. Reconstruction and result analysis.....	25
Results	27
9. Evaluation of modified Pan-Tompkins and template matching algorithms	27
10. Numerical simulation results	27
11. Beat-type triggered vs. retrospectively gated trajectory comparison.....	28
12. Cine beat-type image reconstruction and k-space coverage.....	30
Discussion and Conclusions	34
13. Evaluation of modified Pan-Tompkins and template matching algorithms	34
14. Efficiency comparison between both methods in numerical simulations.....	34
15. Efficiency comparison between both methods in the in-vivo experiment.....	35
16. Comparison between continuous and interleaved segmented sampling trajectories	36
17. Comparison between the proposed method and standard arrhythmia rejection	37
18. Comparison between the proposed method and real-time imaging.....	37
19. Limitations of the proposed methods.....	37
20. Conclusions.....	39

Bibliography40

Curriculum Vitae45

List of Tables

Table 1: Accuracy of heartbeat detection and classification..... 27

List of Figures

Figure 1: ECG recorded within a MRI scanner	7
Figure 2: Pseudocode of modified Pan-Tompkins algorithm	11
Figure 3: Pseudocode of template matching algorithm	13
Figure 4: Heartbeat type classification and trigger generation	17
Figure 5: Sampling trajectories with four radial projections in each segment	18
Figure 6: Difference between data selection of retrospectively gated imaging and triggered beat-type imaging	21
Figure 7: Histogram of the numbers of full premature heartbeats to fully sample k-space using the triggered and retrospectively gated methods	28
Figure 8: k-Space projections of the continuous segmented sampling of the triggered method and the retrospectively gated method	30
Figure 9: Reconstruction of the continuous segmented sampling	32
Figure 10: Reconstruction of the interleaved segmented sampling with golden ratio interleaving	33
Figure 11: Detection of sinus heartbeats.....	38

Introduction

1. Motivation

Breath-hold electrocardiography (ECG) synchronized cine imaging is considered as the standard for assessing cardiac function with cardiac MRI (CMR). However, the image quality of this method is commonly compromised by patients' arrhythmias and inability to hold their breath. Additionally, this method cannot provide cine images of arrhythmias which may also be of interest when evaluating arrhythmia pathophysiology. Real-time CMR is under investigation to solve the problems that currently exist in standard cine imaging [1]–[4]. However, real-time CMR usually has limited temporal and spatial resolution, introduces image artifacts due to under-sampling or motion, and requires sophisticated time-consuming reconstruction methods.

Here, targeting at clinically feasible applications, we implemented a novel triggering method that provides good cine image quality while maintaining high temporal and spatial resolution using clinically feasible reconstruction methods. This method utilized a newly developed scanner triggering system that updates the sampling trajectory in real-time based on the occurrence of a target heartbeat type as observed during free breathing. A retrospectively gated method that selects k-space data based on the post-processed physiological signals was also implemented.

2. Background

Signal excitation

Protons of an object can be magnetized in a magnetic field \mathbf{B}_0 . If \mathbf{B}_0 is static, the macroscopic proton magnetization \mathbf{M} is along the direction of \mathbf{B}_0 that is assumed to be the z-axis. If another magnetic field \mathbf{B}_1 orthogonal to \mathbf{B}_0 is applied to the object for a short period of time, the macroscopic proton magnetization will be tilted away from z-axis and produce magnetization M_{xy} in the x-y plane in a phenomenon called forced precession. The angle between the direction of magnetization and z-axis is called “flip angle”. This \mathbf{B}_1 is normally produced by a radio-frequency signal pulse (RF pulse) whose magnitude is far less than the magnitude of \mathbf{B}_0 (B_0) [5].

The decay of location-dependent magnetization $M_{xy}(\mathbf{r})$ can emit detectable signal in the form as:

$$S(t) = \int_{\text{object}} M_{xy}(\mathbf{r}) e^{-\frac{t}{T_2}} e^{-i\omega(\mathbf{r})t} d\mathbf{r} \quad (1)$$

where the parameter T_2 characterizes the decay speed of $M_{xy}(\mathbf{r})$. $\omega(\mathbf{r})$ is the angular precession frequency of protons:

$$\omega(\mathbf{r}) = \gamma B(\mathbf{r}) \quad (2)$$

where $B(\mathbf{r})$ is a location-dependent magnetic field which performs spatial information

encoding.

Spatial information encoding and k-space

The spatial information of MR signals is encoded to perform imaging. To encode spatial information at location \mathbf{r} , a linearly location-dependent magnetic field:

$$B(\mathbf{r}) = \mathbf{G} \cdot \mathbf{r} \quad (3)$$

should be superimposed on the static magnetic field \mathbf{B}_0 with the same direction (the z-axis). \mathbf{G} is a vector called the gradient.

Two kinds of encoding are available: frequency and phase encoding [6]. Frequency encoding incorporates spatial information into the oscillation frequency of protons of the object. The angular frequency of protons at \mathbf{r} in B_0 plus $\mathbf{G}_{fe} \cdot \mathbf{r}$ is:

$$\omega(\mathbf{r}) = \gamma(B_0 + \mathbf{G}_{fe} \cdot \mathbf{r}) \quad (4)$$

Thus, protons within $d\mathbf{r}$ at location \mathbf{r} generates signal as:

$$dS(\mathbf{r}, t) = \rho(\mathbf{r})e^{-i\gamma(B_0 + \mathbf{G}_{fe} \cdot \mathbf{r})t} d\mathbf{r} \quad (5)$$

where $\rho(\mathbf{r})$ weights the signal at location \mathbf{r} and \mathbf{G}_{fe} is constant from 0 to t .

After demodulation to remove the carrier signal $e^{-i\gamma B_0 t}$, the signal emitted from the entire object is:

$$S(t) = \int_{-\infty}^{+\infty} \rho(\mathbf{r}) e^{-i\gamma \mathbf{G}_{fe} \cdot \mathbf{r} t} d\mathbf{r} \quad (6)$$

In order to encode 2D or 3D spatial information, phase encoding is needed. Phase encoding is performed by turning on a linear gradient \mathbf{G}_{pe} for a short period of time T_{pe} to add a “phase” $\gamma \mathbf{G}_{pe} \cdot \mathbf{r} T_{pe}$ to the signal at location \mathbf{r} :

$$S = \int_{-\infty}^{+\infty} \rho(\mathbf{r}) e^{-i\gamma \mathbf{G}_{pe} \cdot \mathbf{r} T_{pe}} d\mathbf{r} \quad (7)$$

where \mathbf{G}_{pe} is constant from time 0 to T_{pe} .

To write equations (6) and (7) in the form of a Fourier transform, let:

$$\mathbf{k} = \frac{\gamma}{2\pi} (\mathbf{G}_{fe} t + \mathbf{G}_{pe} T_{pe}) \quad (8)$$

The spatial information encoding could be written as:

$$S(\mathbf{k}) = \int_{-\infty}^{+\infty} \rho(\mathbf{r}) e^{-i2\pi \mathbf{k} \cdot \mathbf{r}} d\mathbf{r} \quad (9)$$

The space of vector \mathbf{k} is called *k-space*. k-Space is essentially equivalent to the frequency domain of an image.

If \mathbf{G}_{fe} and \mathbf{G}_{pe} are functions of time, a k-space point \mathbf{k} should be written as:

$$\mathbf{k} = \frac{\gamma}{2\pi} \left(\int_0^t \mathbf{G}_{fe}(\tau) d\tau + \int_0^{T_{pe}} \mathbf{G}_{pe}(\tau) d\tau \right) \quad (10)$$

MRI sequence and k-space sampling trajectory

An MRI sequence includes RF pulses, gradient waveforms, and data acquisition in order to produce a desired MR image [7]. There are a variety of sequences that are available for different purposes; in this study, the steady-state free precession (SSFP) sequence was used. There are several parameters characterizing a sequence, such as repetition time (TR), echo time (TE), flip angle, and receiver or image bandwidth. As these parameters affect the image contrast, signal-to-noise ratio (SNR), scanning time, to name a few, they should be chosen according to specific applications.

The data acquisition scheme or the k-space sampling trajectory is also important in a sequence, as it affects the image contrast, SNR, and image artifacts. There are several k-space trajectory categories, such as radial and Cartesian sampling, to name a few. Radial sampling, the original method of sampling data in MRI, has broad use in cardiac MR imaging (CMR), as it is relatively robust against motion artifacts [3], [7], [8]. If the SSFP sequence is used, sampling is performed along a radial “projection”, a line through the center of k-space, within each TR, and the angle of a projection is updated during scanning to fully cover k-space. For Cartesian sampling, however, a line parallel to a k-space axis is sampled per TR, and the distance between the k-space center and the line is updated during scanning. TR in the SSFP sequence is defined as the time interval between two consecutive excitation RF pulses and is usually minimized to maximize speed and SNR efficiency and minimize imaging artifacts [10].

The field of view (FOV) of an object is the size of the object being imaged. As sampling of k-space is digitized, the intervals between two consecutive k-space samples along the

x-axis Δk_x and along the y-axis Δk_y satisfies:

$$\Delta k_x = \frac{1}{W_x} \quad (11)$$

$$\Delta k_y = \frac{1}{W_y} \quad (12)$$

where $W_x \times W_y$ is the FOV of the object.

Image reconstruction

The MRI signal is sampled in k-space; thus, reconstruction should be performed to get an image of the object of interest. For Cartesian sampling, the fast Fourier transform (FFT) can be used; for radial sampling, however, an algorithm called gridding is typically used before applying the FFT. Gridding resamples the k-space to the Cartesian raster so that FFT reconstruction can be readily applied. In this study, a similar algorithm called non-uniform FFT (NUFFT) is used to reconstruct an image from radially sampled k-space. More details about NUFFT can be found in [11].

In a 2D radial k-space sampling, the number of k-space samples per radial projection N and the FOV $W \times W$ (which is usually a square FOV) determine the spatial resolution of the reconstructed image. Assume the desired spatial resolution is $\Delta x \times \Delta x$; then the following equation is satisfied:

$$\Delta x = \frac{W}{N} = \frac{1}{N\Delta k} \quad (13)$$

where $N \times N$ is the number of pixels in the reconstructed image.

Cine imaging

In CMR, cine imaging is used to get a movie of the beating heart [12]. Due to the relatively low speed of MRI, cine imaging samples data during several continuous heartbeat cycles to achieve complete coverage of k-space. People usually have approximately periodic cardiac cycles, so cine imaging sorts data from several heartbeats into different time frames according to their corresponding phases of the cardiac cycle. The cardiac phase is normally determined using ECG as showed in Figure 1. Without breath-holding, motion of the heart due to breathing can also compromise the image quality; thus, sometimes the breathing signal should also be monitored, and only data sampled during end-expiration, the most stable position from breath to breath in human subjects, should be kept.

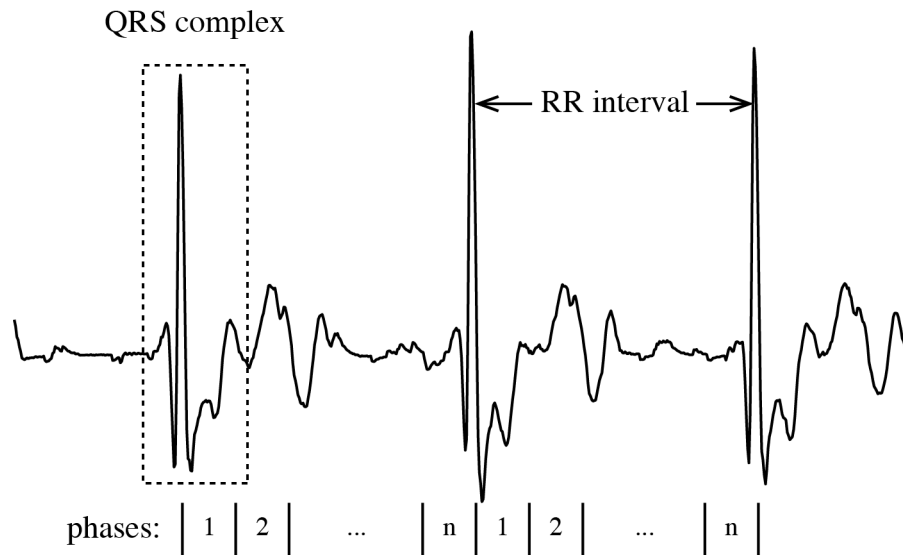


Figure 1: ECG recorded within a MRI scanner (InVivo, Gainesville FL). The MR data are sorted according to their corresponding cardiac phases determined by ECG.

In contrast to the heartbeats (sinus heartbeats) showed in Figure 1, arrhythmias can show different QRS morphology and RR intervals in ECG, due to abnormalities of the heart rate, rhythm, or electrical conduction in the heart [13]. As the heart motion during arrhythmia is no longer consistent, cine imaging can suffer severe image artifacts [2], [13], [14]. A standard method to avoid these artifacts, which can include ghosting and significant streaking, is to reject heartbeats with inconsistent RR intervals at the expense of increased scan duration. However, since arrhythmia affects not only the RR interval but also the morphology in ECG, this method does not provide cine images with high quality. This is one of the reasons that we developed the triggering system described below.

Methods

A scanner triggering system detecting a target heartbeat type (beat-type) and respiratory phase in real-time was developed. If the target beat-type was detected during end-expiration, a trigger was generated and sent to the scanner external input to update the sampling trajectory. This system is new and innovative because it uses more than just the RR interval to classify a heartbeat. By including both QRS morphology, which can vary significantly in the presence of arrhythmia, and respiratory signal monitoring, a more robust triggering system was developed for use in patients with cardiac arrhythmias that currently results in sub-standard cine MRIs. Details of this beat-type triggering system and application to imaging during arrhythmia are described below.

3. Physiologic-signal acquisition

A one-lead analog ECG signal was collected by a clinical MRI ECG monitoring system (InVivo, Gainesville FL), while a respiratory motion waveform was captured by a pneumatic respiratory bellows (BIOPAC system, Inc., Goleta, CA). ECG and respiratory signals were digitized by a commercial data acquisition system (MP150, BIOPAC system, Inc.) and relayed to the real-time heartbeat detection and classification software described below. Additionally, the MRI scanner was programmed to generate a 1 ms rectangular synchronization pulse per TR. This pulse was relayed to the data acquisition system over a fiber-optic connection and recorded along with the physiologic signals to synchronize image acquisition data with the physiologic data.

4. Beat-type detection in real-time and triggering signal generation

Real-time QRS complex detection and beat-type classification software was developed in *Python* with packages *SciPy* (SciPy developers, <http://www.scipy.org>), *Numpy* (NumPy developers, <http://www.numpy.org>), and *matplotlib* [16].

Detection of QRS complexes

QRS complex locations were detected in real-time using a modified Pan-Tompkins algorithm [17]. To detect QRS complexes robustly, the Pan-Tompkins algorithm first uses a series of filters to enhance QRS complexes while suppressing other signals and noise. This algorithm then uses an adaptable threshold to select QRS complexes. Three ways to update the threshold were studied in the work by Hamilton et.al [18]: iterative, mean value, and median value methods. Median value method was used in this work due to the better detection accuracy [18]. This algorithm was modified in the presented work to keep the implementation simple without losing too much detection accuracy [19]. The modified Pan-Tompkins is summarized in Figure 2.

```

1: function DETECTQRSLOCATIONS
2:   qrsLocations  $\leftarrow$  an empty list
3:   for each incoming data point x do
4:     y  $\leftarrow$  preProcess(x)
5:     if y is a peak then
6:       if y > threshold and no QRS found in the last 300 ms then
7:         loc  $\leftarrow$  the timing of x
8:         add loc into qrsLocations
9:       end if
10:      threshold  $\leftarrow$  updateThreshold(y,threshold)
11:    end if
12:  end for
13:  return qrsLocations
14: end function

15: function PREPROCESS(input)
16:   x1  $\leftarrow$  low-pass filter input
17:   x2  $\leftarrow$  high-pass filter x1
18:   x3  $\leftarrow$  differentiate x2
19:   x4  $\leftarrow$  x32
20:   out put  $\leftarrow$  average the 32 most recent x4
21:   return out put
22: end function

23: function UPDATETHRESHOLD(dataPoint, threshold)
24:   if dataPoint > threshold then
25:     define dataPoint as a signal peak
26:   else
27:     define dataPoint as a noise peak
28:   end if
29:   s  $\leftarrow$  the median of 8 most recent signal peaks
30:   n  $\leftarrow$  the median of 8 most recent noise peaks
31:   threshold  $\leftarrow$  0.15s + 2.25n
32:   return threshold
33: end function

```

Figure 2: Pseudocode of modified Pan-Tompkins algorithm

The low-pass, high-pass filters, and differentiation used in this algorithm are specified by the equations (14), (15), and (16), respectively [18].

$$y(n) = x(n) - x(n - 6) + x(n - 12) + 2y(n - 1) - y(n - 2) \quad (14)$$

$$y(n) = y(n - 1) - \frac{1}{32}x(n) + x(n - 16) - x(n - 17) + \frac{1}{32}x(n - 32) \quad (15)$$

$$y(n) = 0.25x(n) + 0.125x(n - 1) - 0.125x(n - 3) - 0.25x(n - 4) \quad (16)$$

Equations (14), (15), and (16) were designed for signals with sampling rate 200 Hz.

Classification of beat-types

Each heartbeat was quantitatively described by a morphology feature and an RR feature. The morphology feature was defined as a 300 ms segment of ECG data around a QRS complex, and the RR feature was defined as the interval between the current and the next QRS complex. Using a template matching algorithm [20], heartbeats were classified into different types based on similarities between their features and the features of template heartbeats. We defined this type as a *local type* in order to be distinguished from the beat-type that this algorithm finally assigned to a certain heartbeat. To enable classification flexibility, template heartbeats were dynamically created from heartbeats that were not sufficiently similar to any available template heartbeats. More details of this algorithm can be found in the pseudocode showed in Figure 3.

```

1: function TEMPLATEMATCHING
2:   set  $T_m$ : morphology threshold
3:   set  $T_R$ : RR threshold
4:    $beatTypes \leftarrow$  a empty list
5:   for each QRS wave do
6:      $candidates \leftarrow$  an empty list
7:      $morphology \leftarrow$  300ms segment around this QRS wave
8:      $RR \leftarrow$  the time between this and the next QRS waves
9:     for each available  $template$  do
10:       $S_m \leftarrow \max \left( \frac{\text{cross-correlation}(morphology, template.morphology)}{\text{norm}(morphology)\text{norm}(template.morphology)} \right)$ 
11:       $S_R \leftarrow \left| \frac{template.RR - RR}{template.RR} \right|$ 
12:      if  $S_m > T_m$  and  $S_R > T_R$  then
13:         $score \leftarrow S_m + S_R$ 
14:        add  $(score, template)$  into  $candidates$ 
15:      end if
16:    end for
17:    if  $candidates$  is not empty then
18:      find the  $template$  associated with the highest  $score$  from  $candidates$ 
19:      add  $template.ID$  into  $beatTypes$ 
20:    else
21:      add  $(morphology, RR)$  as  $newTemplate$ 
22:       $newTemplate.ID =$  total number of available templates  $- 1$ 
23:      add  $newTemplate.ID$  into  $beatTypes$ 
24:    end if
25:  end for
26:  return  $beatTypes$ 
27: end function

```

Figure 3: Pseudocode of template matching algorithm

As ventricular volumes and ejection fraction of the current heartbeat can be affected by the morphology of the previous heartbeat, the beat-type finally assigned to the current

heartbeat was defined as the local type of the current heartbeat in addition to the local type of the previous heartbeat.

Evaluation of QRS complex detection and beat-type classification

The modified Pan-Tompkins and the template matching algorithms were tested on MIT-BIH arrhythmia database [21], [22] with 48 ECG records. Each record is slightly above 30 minutes with 360 Hz sampling frequency. A modified limb lead II (MLII) ECG of each record was used in this test. As the modified Pan-Tompkins algorithm was designed for signals with 200 Hz sampling frequency, linear interpolation was performed to down-sample these records. For the template matching algorithm, the morphology threshold was empirically set to 0.7, and the RR threshold was empirically set to 0.7.

After processing by the modified Pan-Tompkins and the template matching algorithms, the classification results were compared with the reference beat annotations included with these records (the description of beat annotations could be found online in <http://physionet.org/physiobank/annotations.shtml>). To assess the accuracy of the implemented algorithms in the classification of each beat type, the results of classification were mapped to the reference beat annotations, since the template-matching can only discriminate among different types but cannot determine the exact name of a given morphology. To perform the mapping, the timing of the classified heartbeats was compared with the timing heartbeats of each reference annotation, and the reference annotation that included the highest number of heartbeats with the same timing was paired with the beat-type. Finally, the accuracy was calculated as the number of correctly classified heartbeats divided by the total number of heartbeats in the reference

annotations.

Detection of end-expiration

The end-expiratory phase was detected by thresholding of a respiratory bellows signal. Prior to thresholding, a direct current (DC) removal filter [23] (equation (17)) and a Butterworth low-pass filter designed using MATLAB (MathWorks, Inc., Natick, MA. Release 2016a) (equation (18)) were applied to remove the drift and the noise, respectively.

$$y(n) = x(n) - x(n - 1) + 0.995y(n - 1) \quad (17)$$

$$y(n) = 0.0078x(n) + 0.0078x(n - 1) + 0.9844y(n - 1) \quad (18)$$

Equations (17) and (18) were designed for signals with sampling rate 200 Hz.

Trigger generation

The software was also implemented with the functionality that allowed users to change target beat-type in real-time. As the template matching algorithm had no knowledge of the names of different arrhythmias and sinus heartbeats, the users had to be familiar with the ECG morphology of the target beat-type expected to be triggered. When the target beat-type was detected during end-expiration, a 5V trigger pulse was generated (BIOPAC System, Inc.) and applied to the external trigger input of the MRI scanner. The trigger pulse was used to change the k-space sampling location after the whole target heartbeat. Therefore, the effects of the trigger were delayed until the detection of the next QRS

complex.

Figure 4 illustrates classification of heartbeats and a generated trigger pulse in a human subject with premature ventricular complexes (PVCs).

5. Design of imaging sequences

Triggered beat-type imaging sequence design

A conventional segmented radial SSFP sequence was modified to update the sampling trajectory when the MRI scanner received an external trigger pulse. When the triggering option was enabled, the sampling of the same k-space segment was repeated until detection of an external trigger, at which point the sampling was advanced to the next k-space segment. Two sampling trajectories were evaluated in this study: continuous segmented radial sampling [24] and interleaved segmented sampling with golden-ratio interleaving [24], [25] as illustrated in Figure 5 A and B, respectively.

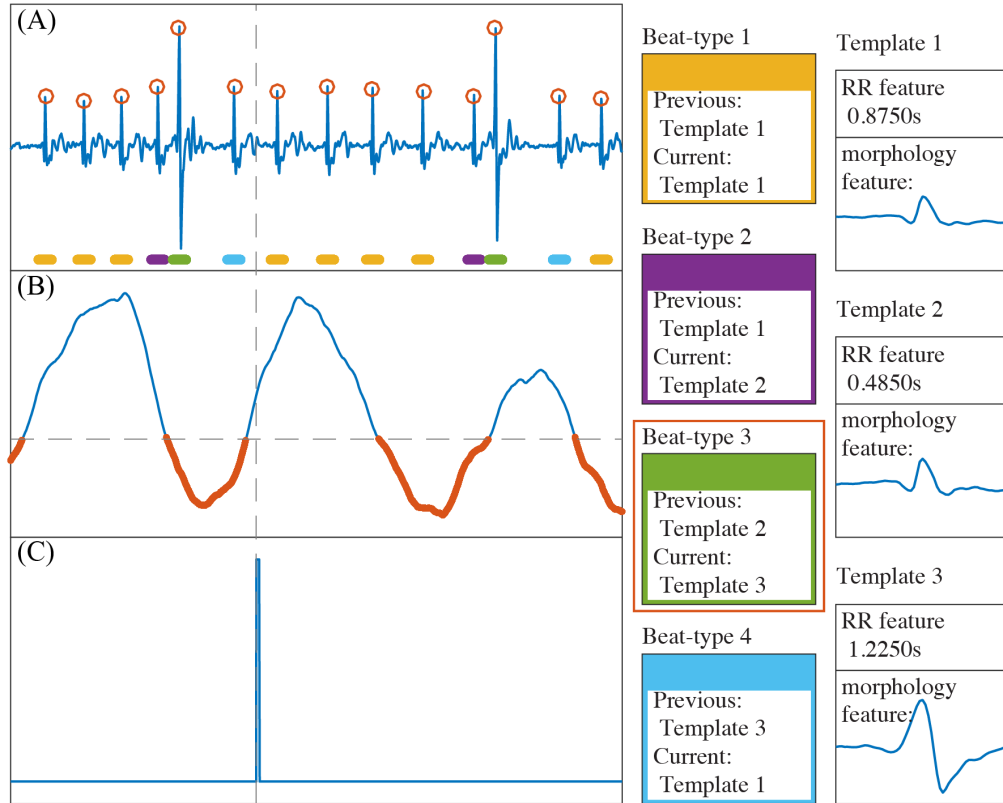


Figure 4: Heartbeat type classification and trigger generation. **A:** Heartbeat type classification. Detected QRS complex locations are marked by red circles, and results of heartbeat type classification are marked by different colors. The green heartbeats (beat-type 3) representing premature ventricular contractions (PVCs) are selected for trigger generation. Three templates with different morphology or RR features are generated. Four heartbeat types formed by different template combinations are detected. **B:** Filtered respiratory signal. Expiratory windows are marked by red. **C:** A trigger generated following the first PVC that occurs within an expiratory window. Notice that no trigger is generated for the second PVC that occurs during inspiration.

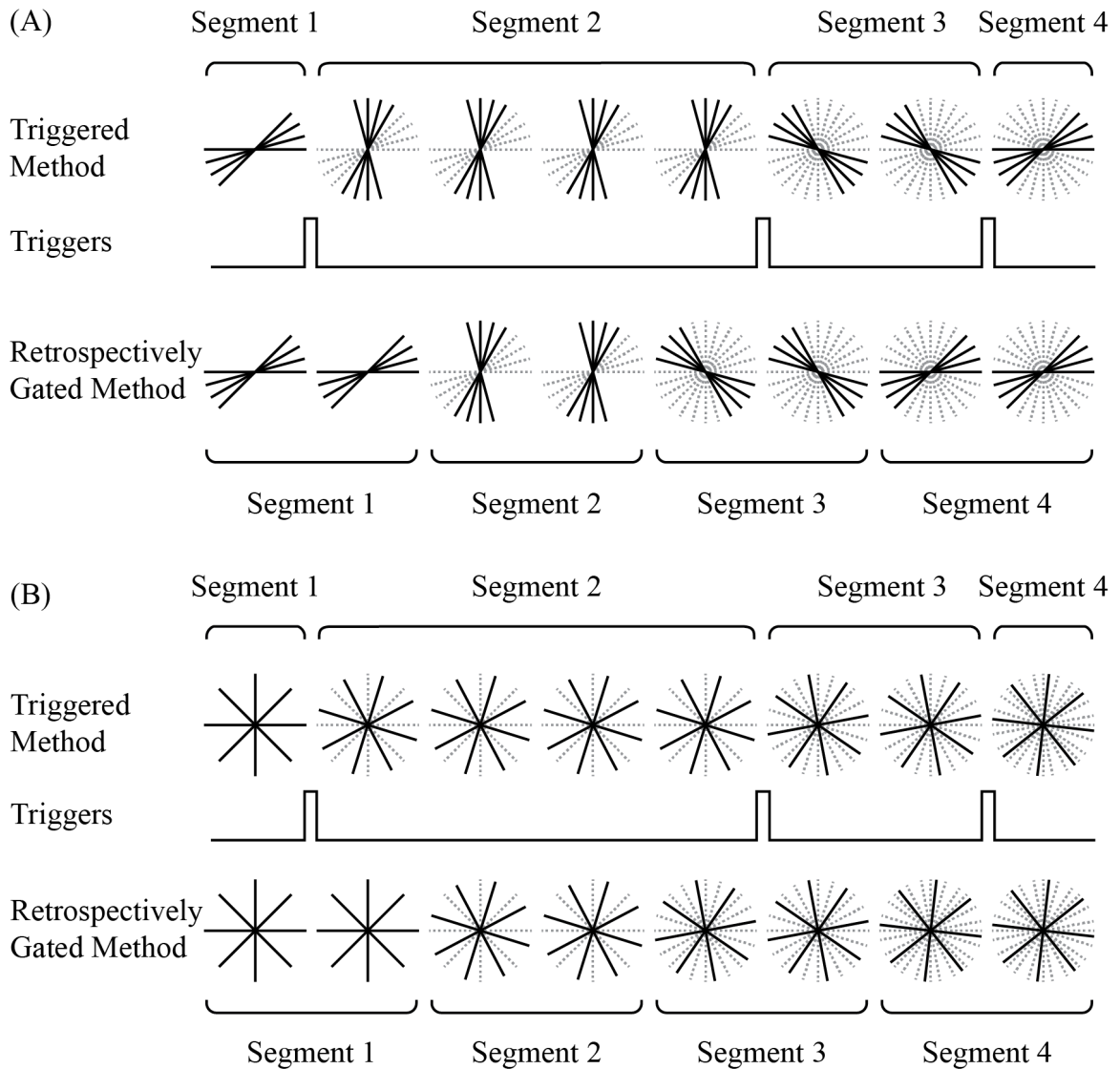


Figure 5: Sampling trajectories with four radial projections in each segment. Sampled projections are plotted using solid lines; previously sampled projections are plotted using dash lines. Using the triggered method, the trajectory is updated when a trigger is received by the scanner. Using retrospective gating, the trajectory is updated after a fixed number of repetitions of the same segment (2 in this case). **A.** Continuous segmented sampling trajectory. **B.** Interleaved segmented sampling trajectory with golden-ratio interleaving.

For the continuous segmented trajectory, the angular spacing between projections within each segment was set to $\frac{\pi}{N_{proj}}$, where N_{proj} was the number of radial projections to fully sample the radial k-space. The first projection of each segment was set to $\frac{\pi(n_{seg}-1)}{N_{seg}}$ where n_{seg} was the current segment number and N_{seg} was the total number of k-space segments. This trajectory was selected to minimize angular spacing between projections in order to reduce eddy current effect which is one of the sources of image artifacts [26].

For interleaved imaging, the angular spacing between projections within each segment was set to $\frac{\pi}{M_{seg}}$, where M_{seg} is the number of radial projection in a segment, providing uniform k-space coverage within a single segment. The first projection of each segment was set according to the golden ratio: $0.618(m_{seg} - 1)\frac{\pi}{M_{seg}}$ modulo $\frac{\pi}{M_{seg}}$, where m_{seg} was the current segment number. As a following segment always split the largest remaining gap among previous segments, golden-ratio interleaving could provide more uniform coverage of k-space after an arbitrary number of segments [25], resulting in more tolerable under-sampling artifact compared with the continuous segmented method.

Retrospectively gated beat-type imaging sequence design

In this study, triggered beat-type imaging was compared to gating with retrospective physiologic signal processing. The same sequence described for triggered imaging was also used in retrospectively gated imaging. However, instead of trigger-based trajectory update, the same k-space sampling segment was repeated a specified number of times before advancing to the next k-space segment. The number of segment repetitions was set

to fill 1.2 times the longest expected RR interval. A brief illustration is also included in Figure 5, where the repetition number equal to 2.

After imaging acquisition, associated physiologic signals were processed offline using the beat-type detection software described above, and the imaging data corresponding to the target beat-type during end-expiration were selected. Regarding data selection, any parts of a target heartbeat during end-expiration could be selected in retrospectively gated imaging; however, in triggered imaging, the whole heartbeat had to fall within an end-expiratory window to be selected, as illustrated in Figure 6.

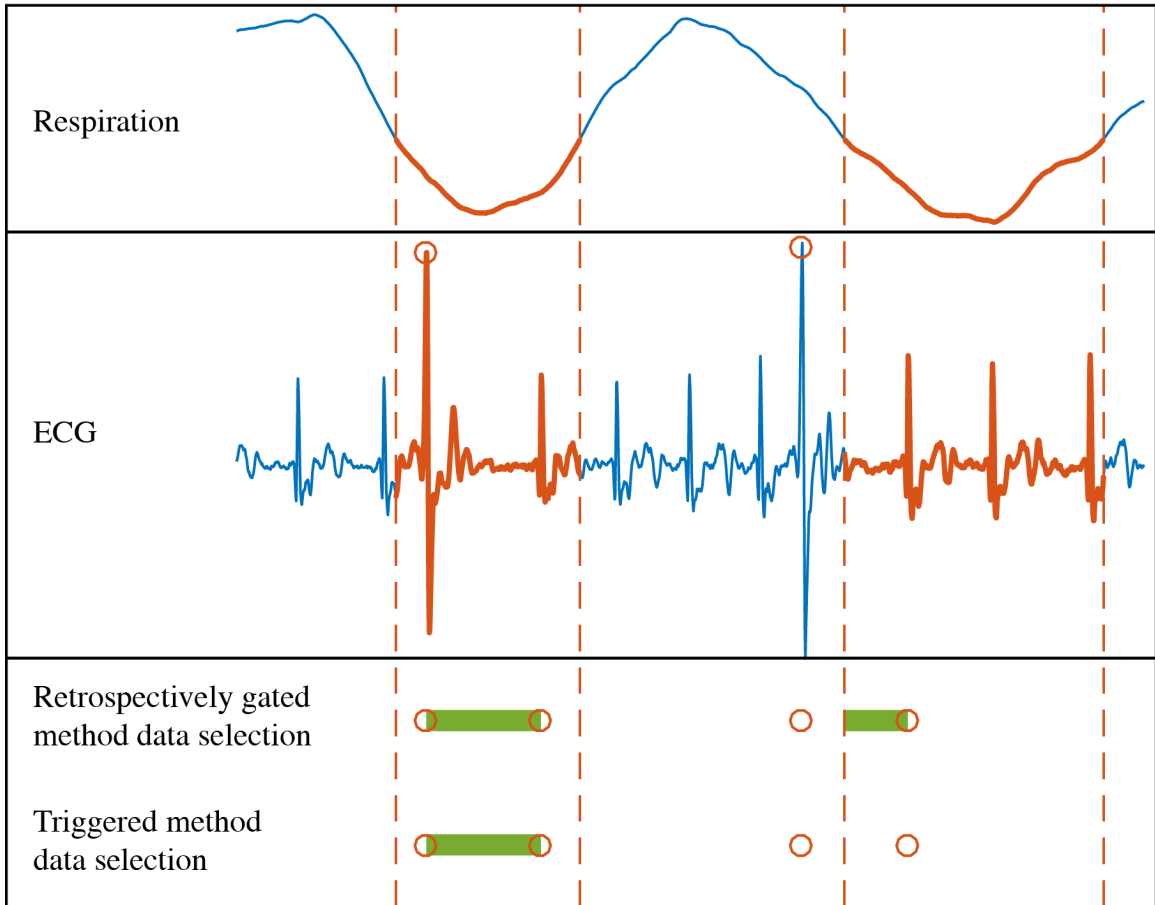


Figure 6: Difference between data selection of retrospectively gated imaging and triggered beat-type imaging. Expiratory windows and detected PVCs are marked on the physiologic signals. The timing of the selected imaging data is marked using green bars. Notice that the whole heartbeat of the first PVC falls within end-expiration. Therefore, the corresponding data segment is selected in both methods. However, only a part of the second PVC falls in end-expiration; thus only retrospectively gated method selects the corresponding data segment.

6. Numerical simulations

To more generally assess the efficiency of beat-type imaging using the triggered and retrospectively gated methods, a numerical simulation was performed. One hour and a half of physiologic signals with sampling frequency 4000 Hz were simulated to achieve fully sampled k-space. ECG waveforms were simulated with baseline heart rates from 60 to 100 bpm (RR intervals equal to 0.60s, 0.65s, 0.70s, ..., 1.00s, 9 types in total) and premature heartbeats were introduced every 1 to 5 heartbeats (5 types in total). The RR interval of the heartbeat prior to a premature heartbeat was set to half of the baseline RR interval, while the RR interval of a premature heartbeat was set to the baseline RR interval. Zero mean Gaussian noise with standard deviation equal to RR interval times 0.1 was introduced. The simulated respiratory rate was varied from 5 to 20 breaths per minute (the lengths of breath cycle equal to 3, 4, 5, ..., 12 s, 10 types in total) with the length of expiration equal to the length of inspiration. Zero mean Gaussian noise with standard deviation equal to the length of breath cycle times 0.1 was also introduced to simulated breath signals. $5 \times 9 \times 10 = 450$ ECG and respiratory combinations were repeated 20 times, resulting $450 \times 20 = 9000$ simulated physiologic signals in total. In addition to physiologic-signal simulation, a scanner synchronization signal was also simulated with the interval between two synchronization pulses equal to 3.1 ms, which was used to synchronize k-space projections to simulated physiologic signals. For each synchronization pulse, the angle of the sampled k-space projection was incorporated following the angle update principle used in continuous segmented sampling trajectory. The number of projections per segment was set to 9 and the number of segments required to fully sample the k-space was set to 15 to match the in-vivo experiments. Cine data

sorting of premature heartbeats during end-expiration were then generated for triggered and retrospectively gated methods.

The number of full premature heartbeats required to fully sample k-space for all cine frames was then compared for both methods, where a “full premature heartbeat” was defined as a premature heartbeat that fully fell within an end-expiratory window as the first selected heartbeat illustrated in Figure 5. According to its principle, triggered imaging guaranteed to use 15 full premature heartbeats to fully sample the k-space, while this number for the retrospectively gated method was indefinite. Meanwhile, we should note that this comparison was inherently biased for the retrospectively gated method, since this method benefited from premature heartbeats that only partially fell within an expiratory window as illustrated in Figure 6.

A one-tailed Wilcoxon rank sum test performed using the MATLAB *ranksum* function (MathWorks, Inc., Natick, MA. Release 2016a) was used to assess the difference between the distributions of the numbers of full premature heartbeats required for triggered and retrospectively gated methods. The null hypothesis was that the two distributions had the same median, and the alternative hypothesis was that the median of the retrospectively gated method was greater than the median of the triggered method.

7. Beat-type imaging experiment design

All animal protocols were reviewed and approved by the Animal Care and Use Committee at the Johns Hopkins University and conformed to the guidelines published in

the “Position of the American Heart Association on Research Animal Use.”

A domestic pig (weight 40 kg) was studied during mechanical ventilation while under general anesthesia. Using X-ray fluoroscopy guidance, a 7 F sheath was inserted into the right internal jugular vein and a non-ferromagnetic pacing catheter was advanced into heart.

The ventilated animals were transferred to a 1.5 T MRI scanner (Avanto, Siemens Medical Systems, Erlangen, Germany) and imaged using the standard chest and spine array coils.

A programmable overdrive pacing stimulus was applied at 10 beats per minutes (bpm) over the base heart rate of the animal (Arduino Uno, <https://www.arduino.cc>). A premature pacing stimulus was delivered every 4th heartbeat to simulate arrhythmia with premature atrial complexes (referred as premature beats below). The pacing stimulus was used to trigger a 5 mA pacing pulse (A385, World Precision Instruments, Inc., Sarasota FL). The pacing pulse was delivered to the intra-cardiac pacing catheter over 64MHz RF filtered coaxial cable to suppress imaging noise and induced RF currents during imaging. ECG and respiratory waveforms were acquired and processed in real-time during imaging. The beat-type trigger pulse was connected to the scanner external trigger input.

For this study, the premature beat was selected as the beat-type of interest for imaging. steady-state free precession (SSFP) imaging of the left ventricle short axis (LV SAX) was performed using the triggered method and the retrospectively gated method described above. Imaging for each method was performed using both continuous segmented

sampling and interleaved segmented sampling with golden-ratio interleaving. Imaging parameters were TR = 3.1 ms, TE = 1.5 ms, flip angle = 60 degrees, FOV = 220 mm x 220 mm, slice thickness = 6 mm, reconstruction image dimensions = 128 pixels x 128 pixels, oversampling factor = 2, spatial resolution = 1.7 mm x 1.7 mm (FOV divided by reconstruction image dimensions), bandwidth = 953 Hz/pixel, projections per segment = 9, and segments per image = 15. The number of projections per segment (= 9) was chosen to fit each imaging segment within a target temporal resolution of less than 30 ms. Scans were performed for 2 minutes for each imaging protocol to ensure full sampling of the premature beat during end-expiration.

8. Reconstruction and result analysis

For comparison, both triggered and retrospectively gated scans were truncated at the time when the first 15 full premature heartbeats were detected. Cine data sorting was then applied to both methods. Finally, each cine phase was reconstructed using non-uniform fast Fourier transform (NUFFT). A 5-neighbor Kaiser-Bessel kernel with min-max interpolator was used. [11]

k-Space coverage and image quality were compared between the triggered and retrospectively gated cine images. Additionally, for continuous segmented sampling, the number of premature heartbeats required to fully sample k-space was compared to assess the relative time efficiency of both methods.

The number of cine phases was chosen as the largest integer that was less than the RR

interval divided by target temporal resolution (given by TR times the projection number per segment = $3.1 \text{ ms} \times 9 = 27.9 \text{ ms}$), thus the actual temporal resolution was RR interval divided by the cine phase number. If more than one projection had the same angle in a given cardiac phase, only the first projection was kept.

Results

9. Evaluation of modified Pan-Tompkins and template matching algorithms

The mean accuracy was 76.03% and the standard deviation is 19.50%. The accuracy for each record is showed in Table 1.

Table 1: Accuracy of heartbeat detection and classification

Record Number	100	101	102	103	104	105	106	107
Accuracy (%)	97.67	70.08	74.90	98.90	77.52	90.51	54.86	78.61
Record Number	108	109	111	112	113	114	115	116
Accuracy (%)	65.97	97.95	95.29	99.80	91.75	43.05	97.13	94.20
Record Number	117	118	119	121	122	123	124	200
Accuracy (%)	99.54	79.19	76.85	97.05	68.30	92.75	90.86	65.71
Record Number	201	202	203	205	207	208	209	210
Accuracy (%)	42.54	49.81	26.31	95.33	64.95	75.16	88.32	46.64
Record Number	212	213	214	215	217	219	220	221
Accuracy (%)	81.11	84.87	80.50	94.35	43.21	74.19	90.72	54.02
Record Number	222	223	228	230	231	232	233	234
Accuracy (%)	32.42	72.82	65.12	67.77	85.93	65.00	71.58	98.47

10. Numerical simulation results

The numbers of full premature heartbeats required to fully cover the k-space for the triggered and retrospectively gated methods are shown in Figure 7. Although the retrospectively gated method requires a minimum of 12 full premature heartbeats to reach

full sampling, the median of the number of full premature heartbeats is 51; however, the triggered method requires a constant 15 full premature heartbeats. $P = 0$.

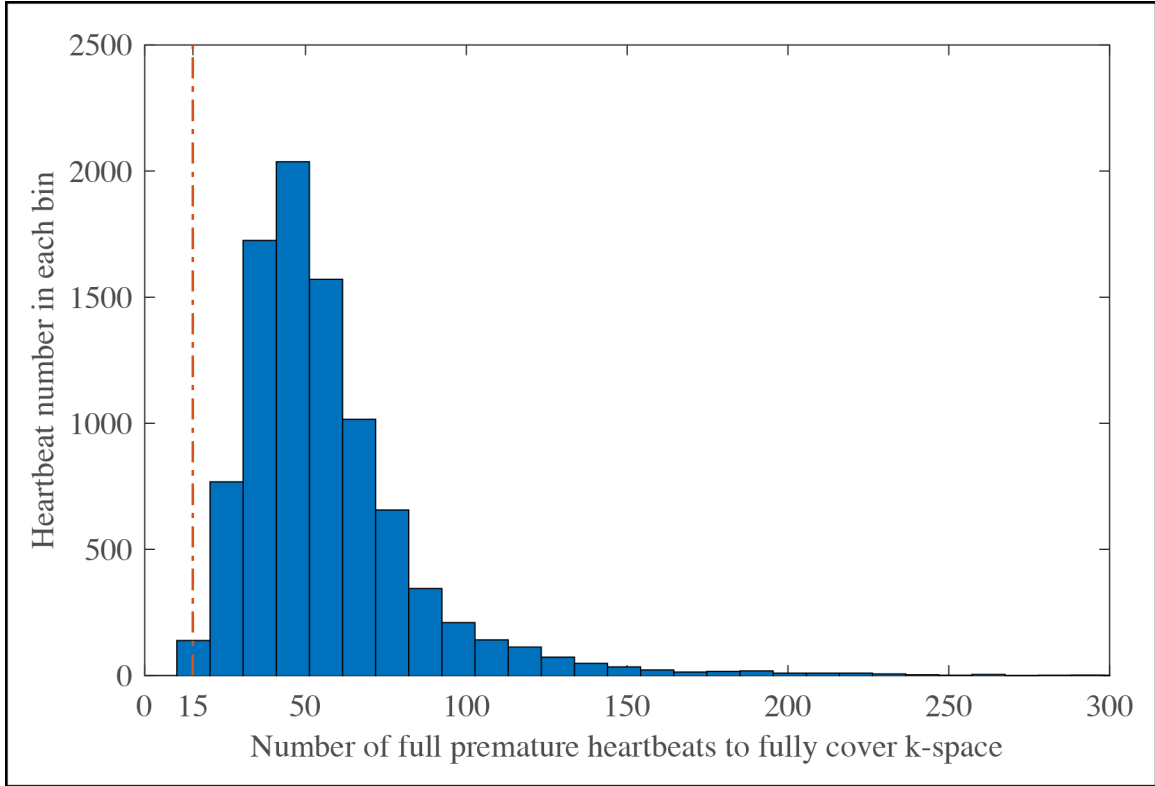


Figure 7: Histogram of the numbers of full premature heartbeats to fully sample k-space using the triggered and retrospectively gated methods. Red dash line indicates the number (15) of full premature heartbeats required by the triggered method. Numbers exceeding 300 are not showed.

11. Beat-type triggered vs. retrospectively gated trajectory comparison

Figure 8 compares the experimental continuous segmented sampling trajectory for the triggered method and the retrospectively gated method. Only the projections for the first

cine phase are shown. The triggered method generates an ascending “step-shaped” sampling pattern that predictably increments without sampling gaps each time the beat-type of interest was encountered. By comparison, the retrospectively gated method has no knowledge of the heart rhythm during imaging and generates a “pseudo-random” sampling pattern when retrospective beat-type and respiratory gating are performed.

For the triggered method, k-space was fully sampled after 15 full premature heartbeats. However, for the retrospectively gated method, k-space had unfilled gaps after 15 full premature heartbeats, and this scan (24 detected premature heartbeats in total) had insufficient data for the retrospectively gated method to fully sample the k-space.

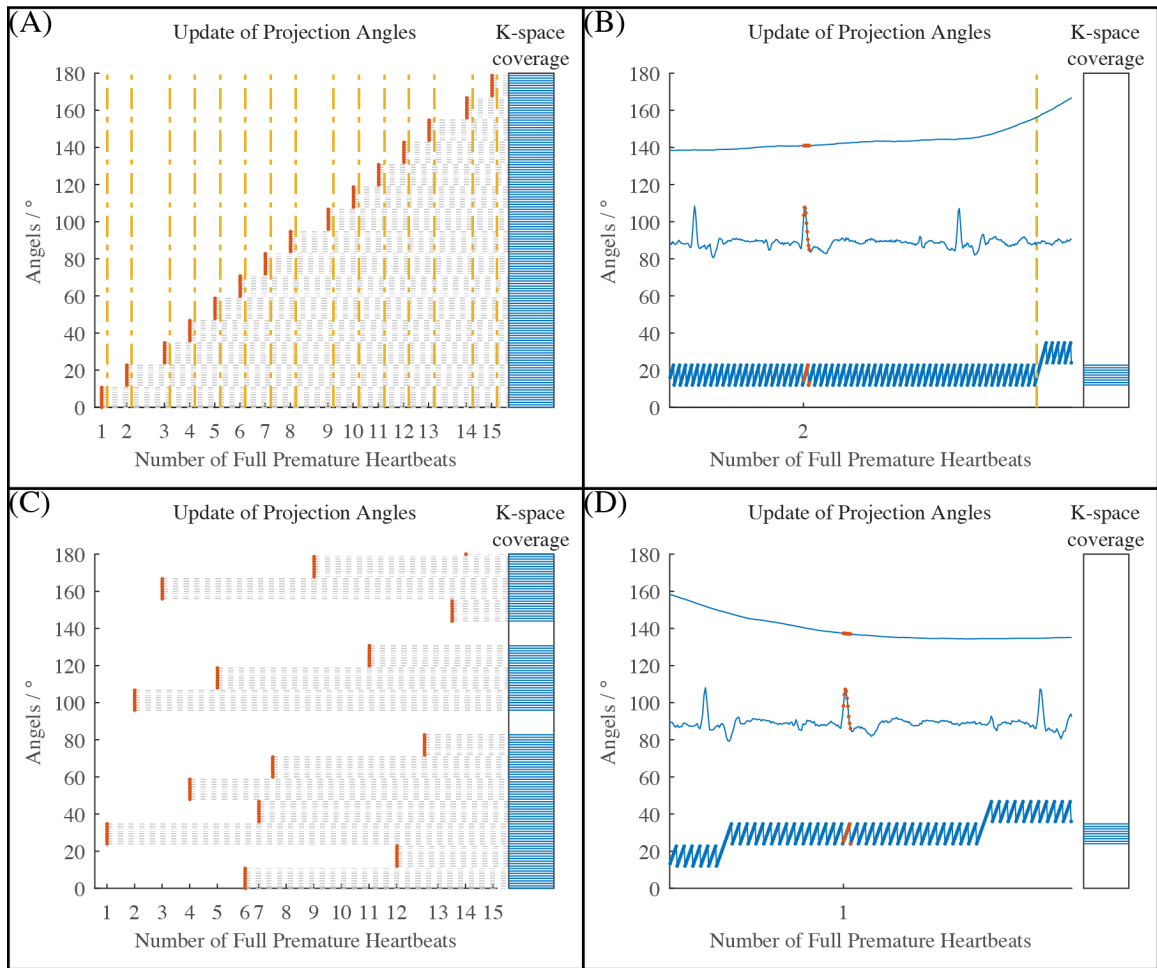


Figure 8: k-Space projections of the continuous segmented sampling of the triggered method (A and B) and the retrospectively gated method (C and D). Red dots represent the selected data for the reconstruction of the first cine phase and corresponding physiologic signals. Vertical yellow dash lines represent triggers. **A, C:** selected projections after 15 full premature heartbeats. **B, D:** physiologic signals and sampled projections during one full premature heartbeats.

12. Cine beat-type image reconstruction and k-space coverage

Figure 9 shows the k-space coverage and the resulting images after the first 15 premature

heartbeats using continuous segmented sampling. End-systolic, mid-diastolic, and end-diastolic cine results are selected from the 25 frame cine image with temporal resolution 28 ms. Full sampling for all cine frames is noted using the triggered method; however, variable gaps are present in the k-space coverage using the retrospectively gated method. Corresponding image artifacts due to under-sampling are seen in the retrospectively gated images.

Figure 10 shows the results for interleaved imaging with golden-ratio interleaves. The end-systolic image is shown after 1, 3, and 5 full detected premature heartbeats for both methods. The k-space coverage is more uniform using the triggered method compared with the retrospectively gated method, reflecting orderly selection of consecutive golden-ratio interleaves. In this case, the under-sampling artifact is less noticeable after 5 premature heartbeats using the triggered method compared with the retrospectively gated method.

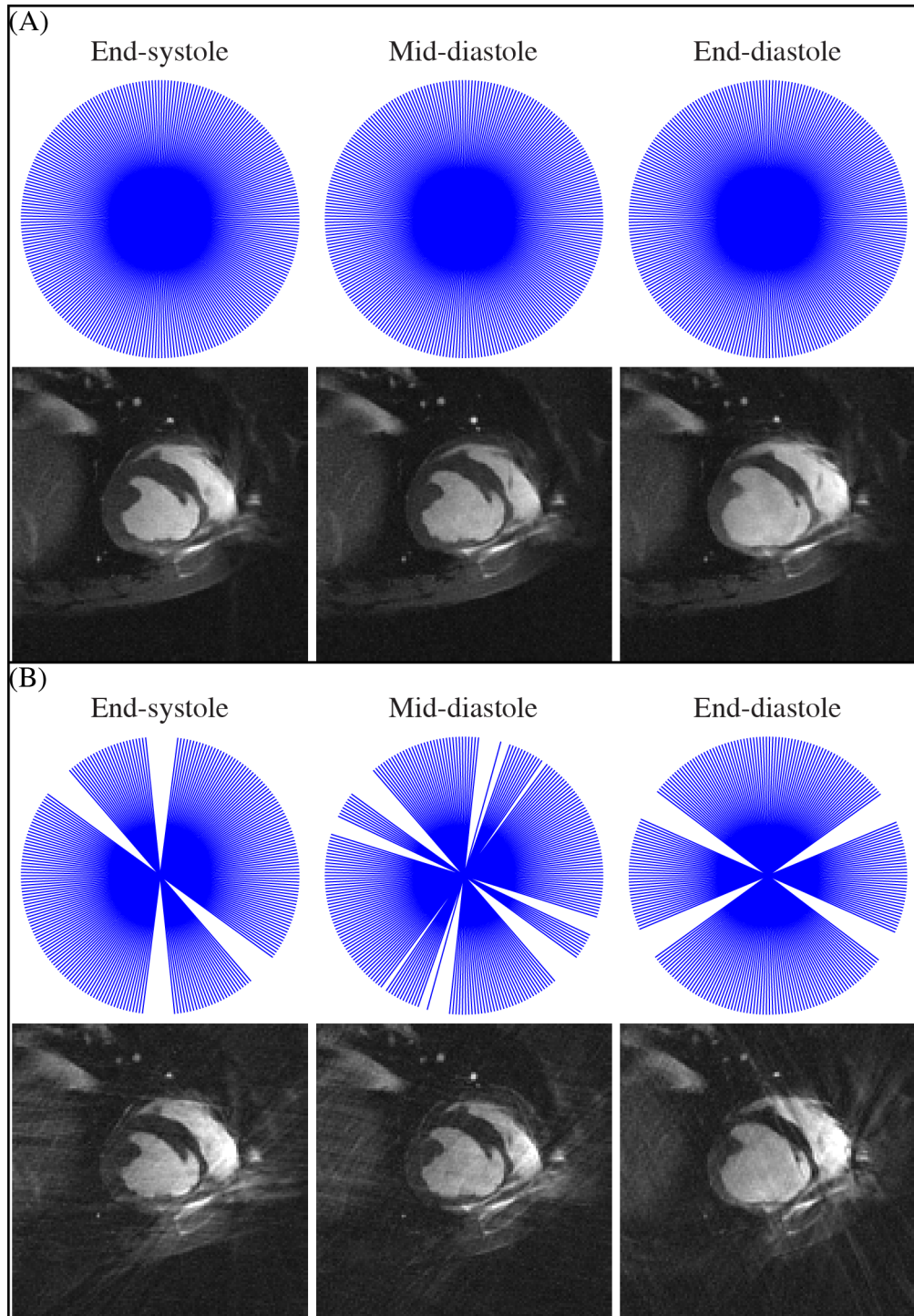


Figure 9: Reconstruction of the continuous segmented sampling. End-systole, mid-diastole, and end-diastole of the cine images are showed. **A.** Triggering method. **B.** Retrospectively gated method.

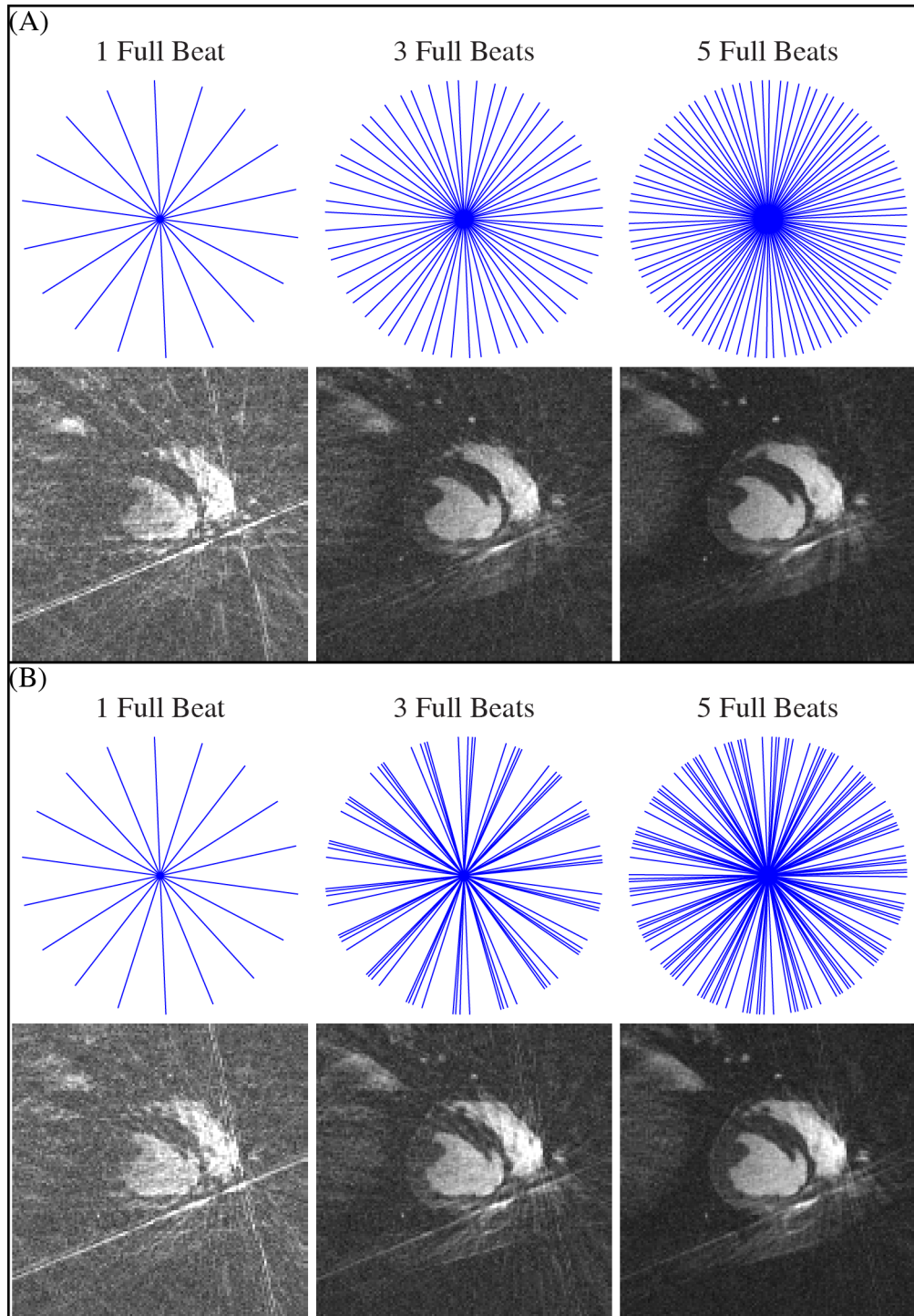


Figure 10: Reconstruction of the interleaved segmented sampling with golden ratio interleaving after 1, 3, and 5 full premature heartbeats. End-systole is shown. **A.** Triggered method. **B.** Retrospectively gated method.

Discussion and Conclusions

13. Evaluation of modified Pan-Tompkins and template matching algorithms

Compared to other beat-type classification algorithms [27]–[30], the template matching algorithm implemented in this study has relatively low accuracy. However, this algorithm does not require training on arrhythmia databases and allows subject-adaptable beat-type classification. Furthermore, morphology and RR thresholds could be adjusted to increase classification accuracy for a specific subject; but this will increase the probability of compromising detection sensitivity of the target beat-type, thus prolonging scanning time. More accurate classification algorithms could be incorporated in the triggering system in the future with the only constraint being that the time available for classification cannot exceed the duration of one heartbeat. To increase the accuracy of real-time heartbeat classification on a variety of different arrhythmias, an ECG system with more leads [31] could be also used.

14. Efficiency comparison between both methods in numerical simulations

The numerical simulations suggest that it is possible that the retrospectively gated method can require fewer full premature heartbeats to fully sample the k-space than the triggered method, since the minimal number of full premature heartbeats is 12 using the

retrospectively gated method, while the number is 15 using triggered method requires. However, the triggered method is more efficient than the retrospectively gated method in general, which is suggested by the median of full premature heartbeats (51) using the retrospectively gated method and the one-tailed Wilcoxon rank sum test. Because of this result, we only conducted one in-vivo experiment to demonstrate the efficiency of the triggered method.

15. Efficiency comparison between both methods in the in-vivo experiment

Because of the fact that the triggered method required less full heartbeats than the retrospectively gated method to fully sample the k-space, the experiment also suggests higher efficiency of the triggered method over the retrospectively gated method. Intuitively, the retrospectively gated method requires fewer full heartbeats, as it also takes advantage of heartbeats that only partially fall within an expiratory window. This is revealed in Figure 10 where the retrospectively gated method has more projections than the triggered method. However, in sampling trajectories that have fixed projection locations in k-space, such as the continuous segmented sampling trajectory, it is difficult for the retrospectively gated method to fill the uncovered k-space “gap” simply by chance (Figure 9); this finding was also suggested by the numerical simulations. In contrast, the triggered method, which only changes the segment of k-space being sampled when the desired beat-type is found, achieves full k-space coverage in a pre-designed sampling pattern, thus guaranteeing complete sampling after a certain number of full heartbeats (15 in the presented work). This disadvantage of the retrospectively gated method is expected

to be more severe when approaching higher resolution or 3D imaging, as more k-space segments are required to obtain fully sampled k-spaces. For trajectories that have flexible projection locations (such as those based on the golden ratio [25]), the experiment also suggests that the triggered method has more uniformly distributed projections compared to the retrospectively gated method. Thus we can conclude that better image quality may be achieved with insufficient scan time as showed in Figure 10.

16. Comparison between continuous and interleaved segmented sampling trajectories

The continuous segmented sampling trajectory and the interleaved segmented sampling trajectory with golden-ratio interleaving sampling have different advantages. One of the main reasons for choosing continuous segmented sampling is that it minimizes eddy currents when using the SSFP sequence. This is because the largest angular space between two consecutive projections does not exceed the angular space of a k-space segment ($1.33 \times (9 - 1) = 10.54$ degrees in the presented work). In contrast, in the interleaving sampling trajectory, the largest angular space between two consecutively projections is $180 / 9 = 20$ degrees. On the other hand, the interleaved segmented sampling with golden ratio is more efficient when the scanning time is insufficient. As each segment is spread evenly to cover the whole k-space, and the golden-ratio fashion ensures that the next segment splits the largest k-space “gap” [25], the images have better quality compared with continuous segmented sampling Figure 9 and Figure 10.

17. Comparison between the proposed method and standard arrhythmia rejection

Compared with the standard arrhythmia rejection cine imaging, the proposed method allows users to choose a specific heartbeat type to image. This enables not only accurate arrhythmia-free imaging but also imaging during a specific arrhythmia heartbeat type (such as PVC). The proposed method permits image-based studies of specific arrhythmia pathophysiology for the first time.

18. Comparison between the proposed method and real-time imaging

Compared with real-time imaging [1]–[4], the proposed method (utilizing segmented sampling trajectories and cine imaging) provides the possibility of choosing higher temporal and spatial resolution. Theoretically, the temporal resolution is equal to the acquisition time of a k-space segment thus could be set to any value that is no less than TR (3.1 ms in the presented work) with the trade-off of scanning time. Higher spatial resolution is also achievable, although it would increase TR and the segment number to fully sample k-space. Additionally, the proposed methods use straightforward and fast reconstruction (NUFFT), which is feasible for clinical application.

19. Limitations of the proposed methods

The presented work has limitations. First, the experiment has a very small sample size as only one animal was imaged. However, the observation of higher efficiency of the

triggered method compared with the retrospectively method was also supported by the results from numerical simulations (Figure 7), assuming beat-types can be detected accurately. Another limitation is that the real-time beat-type detection platform was not tested on human subjects. Human subjects could have more inconsistent respiration and different types of arrhythmias compared with the controlled animals, which would increase the complexity of QRS complex detection and beat-type classification.

Third, the current implementation of the real-time beat-type detection software is inefficient when imaging the types of heartbeats that occurred consecutively, such as sinus beats. Considering the following situation illustrated in Figure 11:

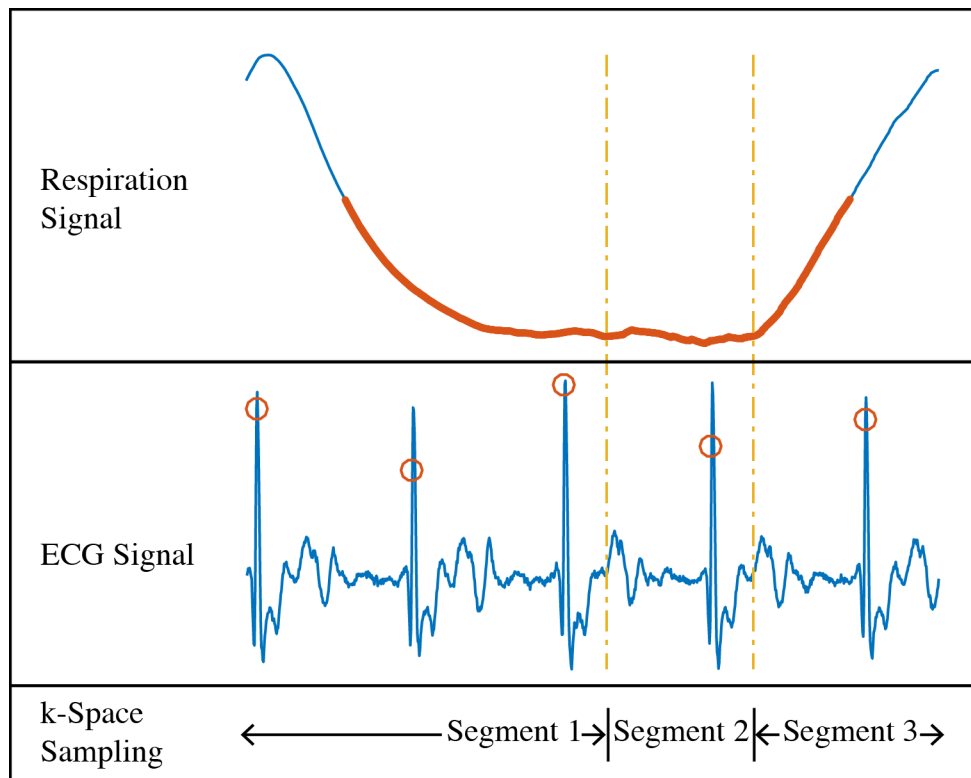


Figure 11: Detection of sinus heartbeats. End-expiration is marked by red in respiration

signal; QRS complex locations are marked by red circles. Notice that the delays between trigger pulses and QRS complexes cause overlapped sampling in k-space.

Due to the delay between the trigger pulse and the QRS complex following the detected heartbeat, if two target heartbeats are detected consecutively as illustrated in Figure 11, the sampling during the delay is identical to the previous sampling, creating gaps in k-space coverage of the first few cine phases. A workaround solution of the proposed method disabled the trajectory update when the consecutive target heartbeat was detected, which compromised the time efficiency. Although this problem could be solved by minimizing this delay by detecting QRS complexes using direct thresholding instead of Pan-Tompkins algorithm, detection flexibility could be compromised.

20. Conclusions

The proposed work provides a platform to perform efficient cine imaging of cardiac arrhythmias with relatively high temporal and spatial resolution, thus enabling the study of arrhythmia pathophysiology using MRI. More efficient methods may be developed and tested on the presented triggering system, especially when applied to high resolution and 3D imaging.

Bibliography

- [1] M. Uecker, S. Zhang, D. Voit, A. Karaus, K.-D. Merboldt, and J. Frahm, “Real-time MRI at a resolution of 20 ms,” *NMR Biomed.*, vol. 23, no. 8, pp. 986–994, 2010.

- [2] L. Feng, M. B. Srichai, R. P. Lim, A. Harrison, W. King, G. Adluru, E. V. R. Dibella, D. K. Sodickson, R. Otazo, and D. Kim, “Highly accelerated real-time cardiac cine MRI using k-t SPARSE-SENSE,” *Magn. Reson. Med.*, vol. 70, no. 1, pp. 64–74, 2013.

- [3] X. Feng, M. Salerno, C. M. Kramer, and C. H. Meyer, “Non-Cartesian balanced steady-state free precession pulse sequences for real-time cardiac MRI,” *Magn. Reson. Med.*, 2015.

- [4] O. Sayin, H. Saybasili, M. M. Zviman, M. Griswold, H. Halperin, N. Seiberlich, and D. A. Herzka, “Real-time free-breathing cardiac imaging with self-calibrated through-time radial GRAPPA,” *Magn. Reson. Med.*, 2016.

- [5] Z.-P. Liang and P. C. . Lauterbur, “Signal Generation and Detection,” in *Principles of magnetic resonance imaging: a signal processing perspective*, New York: IEEE Press, 2000, pp. 57–100.

- [6] Z.-P. Liang and P. C. Lauterbur, “Signal Localization,” in *Principles of magnetic resonance imaging: a signal processing perspective*, New York: IEEE Press, 2000,

pp. 141–180.

- [7] M. A. Bernstein, K. F. King, and X. J. Zhou, *Handbook of MRI pulse sequences*. Elsevier Academic Press, 2004.
- [8] G. H. Glover and J. M. Pauly, “Projection reconstruction techniques for reduction of motion effects in MRI,” *Magn. Reson. Med.*, vol. 28, no. 2, pp. 275–289, 1992.
- [9] S. Pflugi, S. Roujol, M. Akçakaya, K. Kawaji, M. Foppa, B. Heydari, B. Goddu, K. Kissinger, S. Berg, W. J. Manning, and others, “Accelerated cardiac MR stress perfusion with radial sampling after physical exercise with an MR-compatible supine bicycle ergometer,” *Magn. Reson. Med.*, vol. 74, no. 2, pp. 384–395, 2015.
- [10] S. B. Reeder, D. A. Herzka, and E. R. McVeigh, “Signal-to-noise ratio behavior of steady-state free precession,” *Magn. Reson. Med.*, vol. 52, no. 1, pp. 123–130, 2004.
- [11] J. A. Fessler and B. P. Sutton, “Nonuniform fast Fourier transforms using min-max interpolation,” *Signal Process. IEEE Trans.*, vol. 51, no. 2, pp. 560–574, 2003.
- [12] E. R. McVeigh and E. Atalar, “Cardiac tagging with breath-hold cine MRI,” *Magn. Reson. Med.*, vol. 28, no. 2, pp. 318–327, 1992.
- [13] A. Tsiperfal, L. K. Ottoboni, S. Beheiry, A. Al-Ahmad, A. Natale, and P. Wang, *Cardiac arrhythmia management: A practical guide for nurses and allied professionals*. John Wiley & Sons, 2011.

- [14] A. B. Kerr, J. M. Pauly, B. S. Hu, K. C. Li, C. J. Hardy, C. H. Meyer, A. Macovski, and D. G. Nishimura, "Real-time interactive MRI on a conventional scanner," *Magn. Reson. Med.*, vol. 38, no. 3, pp. 355–367, 1997.
- [15] S. Plein, W. H. T. Smith, J. P. Ridgway, A. Kassner, D. J. Beacock, T. N. Bloomer, and M. U. Sivananthan, "Qualitative and quantitative analysis of regional left ventricular wall dynamics using real-time magnetic resonance imaging: Comparison with conventional breath-hold gradient echo acquisition in volunteers and patients," *J. Magn. Reson. Imaging*, vol. 14, no. 1, pp. 23–30, 2001.
- [16] J. D. Hunter and others, "Matplotlib: A 2D graphics environment," *Comput. Sci. Eng.*, vol. 9, no. 3, pp. 90–95, 2007.
- [17] J. Pan and W. J. Tompkins, "A real-time QRS detection algorithm.," *IEEE Trans. Biomed. Eng.*, vol. 32, no. 3, pp. 230–6, Mar. 1985.
- [18] P. S. Hamilton and W. J. Tompkins, "Quantitative investigation of QRS detection rules using the MIT/BIH arrhythmia database," *Biomed. Eng. IEEE Trans.*, no. 12, pp. 1157–1165, 1986.
- [19] Hamilton P. and Tompkins W., "Quantitative investigation of QRS detection rules using the MIT/BIH arrhythmia database," *IEEE Trans. Biomed. Eng.*, vol. BME-33, no. 12, pp. 1157–1165, 1986.
- [20] S. Theodoridis, A. Pikrakis, K. Koutroumbas, and D. Cavouras, *Introduction to Pattern Recognition: A Matlab Approach: A Matlab Approach*. Academic Press,

2010.

- [21] G. B. Moody and R. G. Mark, “The impact of the MIT-BIH arrhythmia database,” *Eng. Med. Biol. Mag. IEEE*, vol. 20, no. 3, pp. 45–50, 2001.
- [22] A. L. Goldberger, L. A. N. Amaral, L. Glass, J. M. Hausdorff, P. C. Ivanov, R. G. Mark, J. E. Mietus, G. B. Moody, C.-K. Peng, and H. E. Stanley, “Physiobank, physiotoolkit, and physionet components of a new research resource for complex physiologic signals,” *Circulation*, vol. 101, no. 23, pp. e215–e220, 2000.
- [23] R. G. Lyons, *Understanding digital signal processing*. Pearson Education, 2011.
- [24] A. Shankaranarayanan, O. P. Simonetti, G. Laub, J. S. Lewin, and J. L. Duerk, “Segmented k-Space and Real-Time Cardiac Cine MR Imaging with Radial Trajectories,” *Radiology*, vol. 221, no. 3, pp. 827–836, 2001.
- [25] S. Winkelmann, T. Schaeffter, T. Koehler, H. Eggers, and O. Doessel, “An optimal radial profile order based on the Golden Ratio for time-resolved MRI,” *Med. Imaging, IEEE Trans.*, vol. 26, no. 1, pp. 68–76, 2007.
- [26] O. Bieri, M. Markl, and K. Scheffler, “Analysis and compensation of eddy currents in balanced SSFP,” *Magn. Reson. Med.*, vol. 54, no. 1, pp. 129–137, 2005.
- [27] S. Osowski and T. H. Linh, “ECG beat recognition using fuzzy hybrid neural network,” *Biomed. Eng. IEEE Trans.*, vol. 48, no. 11, pp. 1265–1271, 2001.

- [28] P. De Chazal, M. O. Dwyer, and R. B. Reilly, “Automatic classification of heartbeats using ECG morphology and heartbeat interval features,” *Biomed. Eng. IEEE Trans.*, vol. 51, no. 7, pp. 1196–1206, 2004.
- [29] Y. Kutlu and D. Kuntalp, “A multi-stage automatic arrhythmia recognition and classification system,” *Comput. Biol. Med.*, vol. 41, no. 1, pp. 37–45, 2011.
- [30] M. Llamedo and J. P. Martínez, “An automatic patient-adapted ECG heartbeat classifier allowing expert assistance,” *Biomed. Eng. IEEE Trans.*, vol. 59, no. 8, pp. 2312–2320, 2012.
- [31] Z. T. H. Tse, C. L. Dumoulin, G. D. Clifford, J. Schweitzer, L. Qin, J. Oster, M. Jerosch-Herold, R. Y. Kwong, G. Michaud, W. G. Stevenson, and others, “A 1.5 T MRI-conditional 12-lead electrocardiogram for MRI and intra-MR intervention,” *Magn. Reson. Med.*, vol. 71, no. 3, pp. 1336–1347, 2014.

Curriculum Vitae

Shuo Han

Birth Date: February 10, 1991

Birth Location: Linyi, Shanxi, China

Education

Johns Hopkins University, Baltimore, MD. Sept. 2014–May. 2016

M.S.E. in Biomedical Engineering

Tsinghua University, Beijing, China. Sept. 2010--Jul. 2014

B.Eng. in Biomedical Engineering

Minor in Computer Technology and Application

Research Experience

**Johns Hopkins University School of Medicine, Dynamic Imaging Laboratory,
Baltimore, MD**

1. Cardiac MRI Heartbeat-Type Triggering System During Arrhythmia

(Jan. 2015–May. 2016)

Implemented software for real-time heartbeat-type classification using unsupervised machine learning, which was integrated into newly developed magnetic resonance imaging (MRI) triggering system to enable clinical MRI of patients with arrhythmia.

Principal Investigator: Aravindan Kolandaivelu.

2. Polyhedral Phantom Framework with Analytical Fourier Transform

(Sept. 2014–May. 2016)

Built highly efficient toolbox for analytical polyhedral Fourier transform to enable realistic and accurate MRI simulations with physiologically relevant shapes and extended mathematical and software framework to include non-uniform intensities. Principal Investigator: Daniel A. Herzka.

3. Highly Accelerated Real-Time T2-Weighted Imaging with Radial GRAPPA

(Sept. 2013)

Provided framework for MRI sequence signal simulation and image reconstruction and compared T2-contrast performance of three MRI sequences. Principal Investigator: Daniel A. Herzka.

Tsinghua University, Center for Biomedical Imaging Research, Beijing, China

1. Unsupervised Machine Learning Based Motion Compensation in MRI

(Jul. 2013–Jun. 2014)

Provided framework for unsupervised machine learning classification of MRI data with physiologic motion, multiplex SENSE image reconstruction, and two quantitative image quality evaluation methods. Principal Investigator: Rui Li.